

RESEARCH ARTICLE

10.1029/2018JB016215

Key Points:

- Friction-permeability relationships are investigated for fractures fabricated with controlled roughness amplitude and wavelength
- Roughness patterns of fracture exert a strong control on permeability evolution via alternating compaction and dilation during shearing
- Rough fractures show high frictional stability initially and stability decreases with shearing, suggesting an aseismic to seismic transition

Correspondence to:

Y. Fang,  
yi.fang@utexas.edu

Citation:

Fang, Y., Elsworth, D., Ishibashi, T., & Zhang, F. (2018). Permeability evolution and frictional stability of fabricated fractures with specified roughness. *Journal of Geophysical Research: Solid Earth*, 123, 9355–9375. <https://doi.org/10.1029/2018JB016215>

Received 11 JUN 2018

Accepted 30 SEP 2018

Accepted article online 4 OCT 2018

Published online 5 NOV 2018

Permeability Evolution and Frictional Stability of Fabricated Fractures With Specified Roughness

Yi Fang<sup>1,2</sup>, Derek Elsworth<sup>2,3</sup>, Takuya Ishibashi<sup>2,4</sup>, and Fengshou Zhang<sup>5</sup>

<sup>1</sup>Institute for Geophysics, Jackson School of Geosciences, The University of Texas at Austin, Austin, TX, USA, <sup>2</sup>Department of Energy and Mineral Engineering, EMS Energy Institute, and G3 Center, The Pennsylvania State University, University Park, PA, USA, <sup>3</sup>Department of Geosciences, EMS Energy Institute, and G3 Center, The Pennsylvania State University, University Park, PA, USA, <sup>4</sup>Fukushima Renewable Energy Institute, National Institute of Advanced Industrial Science and Technology, Koriyama, Japan, <sup>5</sup>Department of Geotechnical Engineering, Tongji University, Shanghai, China

**Abstract** Roughness is widely observed on natural fractures, and its impact on the potential for induced seismicity and associated fluid migration in the subsurface remains unclear. Here we perform fracture shearing and fluid flow experiments on artificially fabricated fractures with specified roughness to investigate the role of fracture roughness on frictional properties and permeability evolution. Given the experimental conditions, we observe that rough fractures show high roughness ratio  $S_q/L_w$  and return higher frictional strength due to the presence of cohesive interlocking asperities. Rough fracture surfaces show velocity strengthening behavior in the initial shearing stage, which may evolve to velocity neutral and velocity weakening at greater displacements—suggesting a dynamic weakening that rough fractures become less stable with shearing. The surface roughness exerts a dominant control on permeability evolution over the entire shearing history. Permeability declines monotonically by about 2 orders of magnitude for smooth fractures. For high roughness fractures, the permeabilities evolve episodically due to cycled compaction and dilation during shearing. With a slip distance of 6 to 8 mm, permeability of the rough surface may enhance up to an order of magnitude, but significant permeability reduction may also occur for rough samples when asperities are highly worn with gouge clogging flow paths. However, there is no obvious correlation between permeability evolution and frictional behavior for rough fracture samples when fractures are subject to sudden sliding velocity changes.

1. Introduction

Recent industrial activities, such as stimulation and production of hydrocarbon reservoirs, enhanced geothermal systems, and wastewater disposal, have been recognized to induce seismicity due to massive fluid injection (Elsworth, 2013; Fang et al., 2016; Majer et al., 2007; Moeck et al., 2009; Walsh & Zoback, 2015; Zoback et al., 2012). Geological carbon sequestration, as a CO<sub>2</sub> mitigation technology, also involves large-scale CO<sub>2</sub> fluid injection, which may induce seismicity and threaten the integrity of caprock formations for long term CO<sub>2</sub> storage (Zoback & Gorelick, 2012). Induced seismicity occurs as seismic slip, slow slip, and aseismic slip (Cornet et al., 1997; Guglielmi et al., 2015; Zoback et al., 2012), which may result in shear compaction or dilation of fractures or faults and lead to permeability reduction or enhancement (Barton et al., 1985; Elsworth & Goodman, 1986; Faoro et al., 2009; Maini, 1972; Segall & Rice, 1995; Ye & Ghassemi, 2018). Hence, understanding permeability evolution with respect to shear deformations is a key step for optimizing the stimulation and production of unconventional reservoirs and for protecting the geological sealing of fluid disposal repositories.

It has long been recognized that these shear deformations result from the reactivation of preexisting fractures or faults due to the increased fluid pressure (Segall & Fitzgerald, 1998; Talwani, 1997). This physical process can be simply described by the Coulomb-Mohr criterion as

$$\tau = C_0 + \mu(\sigma_n - P_f) \tag{1}$$

where  $\tau$  is shear stress,  $C_0$  is cohesive strength,  $\mu$  is the coefficient of friction (also known as the frictional strength),  $\sigma_n$  is normal stress applied on the fracture or fault plane, and  $P_f$  is fluid pressure acting on the fracture wall. When fluid pressure increases, the effective normal stress on a preexisting fault surface is

reduced, making it possible for the fault to slip. When the fault is reactivated at the beginning of slip, the fault movement is governed by the dynamic frictional behavior of the fault contact within the fault. This frictional behavior may be empirically defined by the experimentally derived rate-and-state friction theory (Dieterich, 1978, 1979; Ruina, 1983), in which the dynamic friction coefficient  $\mu$  is written as

$$\mu = \mu_0 + a \cdot \ln\left(\frac{V}{V_0}\right) + b \cdot \ln\left(\frac{V_0 \theta}{D_c}\right) \quad (2)$$

$$\frac{d\theta}{dt} = 1 - \frac{V\theta}{D_c} \quad (3)$$

where  $\mu_0$  is a reference steady state friction at a fault slip velocity  $V_0$ . When the slip velocity increases to  $V$ , the coefficient of friction  $\mu$  instantaneously increases due to the velocity-dependent direct effect scaled by a dimensionless parameter  $a$  and evolves to a new steady state as controlled by the displacement-dependent effect scaled by dimensionless parameter  $b$ .  $\theta$  is a state variable, interpreted as the average lifetime of frictional contacts, and  $D_c$  is the critical slip distance over which a new steady state is achieved. For a finite step in velocity, frictional stability is therefore partially determined by the parameter ( $a-b$ ) as

$$a - b = \frac{\Delta\mu_{ss}}{\Delta \ln V} \quad (4)$$

where  $\Delta\mu_{ss}$  is the difference of static friction prior to and after the velocity change, while ( $a-b$ ) is the friction parameter for evaluating the seismogenic potential of faults or fractures (Rice & Ruina, 1983). Positive ( $a-b$ ) values denote velocity strengthening behavior, which indicates an increase in shear strength with increasing strain rate and results in stable/aseismic slip. Negative ( $a-b$ ) values, on the other hand, indicate velocity weakening behavior and are a prerequisite for unstable/seismic slip.

Recent fracture shearing and fluid flow experiments on shale fractures indicate that permeability evolution of fractures can be linked to the frictional strength and stability because all of these physical parameters are controlled by the solid-solid contact of fracture surfaces during shearing. At low effective normal stress, phyllosilicate-rich shale exhibits weaker frictional strength but much stronger frictional stability and larger permeability reduction than that of carbonate-rich shales (Fang et al., 2017). The permeability evolution is due to the competition between the production of wear products and fracture dilation, which depends on material strength and brittleness—strong-brittle asperities may result in higher frictional strength, lower frictional stability, and larger permeability than that of weak-ductile asperities. However, these conclusions may only reflect the friction-stability-permeability relationship at low confining stresses for fractures with low roughness with asperity size of the order of micrometers. Previous shear deformation experiments suggest that fracture roughness on the order of millimeters may play a different role in controlling the shear deformation and shear strength (Barton, 1973; Barton & Choubey, 1977). That is, when points of contact exist for the two fracture surfaces, the surface roughness can in fact control the fracture aperture, leading to significant dilation. The shearing of “sawtooth” fractures indicates that the sliding occurs on intact asperities at low effective normal stress and results in strong shear dilation and higher increases in permeability. But under high effective normal stress, the intact asperities may shear-off, reducing both shear dilation and permeability (Barton et al., 1985). In addition, the mechanical behavior of fractures is largely dependent on the geometric attributes of asperities, including shape, size, and their spatial distribution on the fracture surface. Thus, the frictional strength and stability and permeability evolution may be controlled by the geometric pattern of asperities. To understand the role of surface roughness, we perform fracture shearing and fluid flow experiments on fractured samples with synthetic patterns of roughness. These samples are fabricated with the assistance of 3-D printing.

This study is organized as follows. First, we design a simple roughness pattern as analogous to that for natural fractures. Then we cast the fracture samples with known statistical roughness features (in terms of asperity height and wavelength) and we perform fracture shearing and fluid flow experiments to measure the frictional strength, stability, and permeability evolution of those roughness-featuring fractures. We finally report the results and discuss how the controlled surface roughness influences frictional stability and permeability evolution.

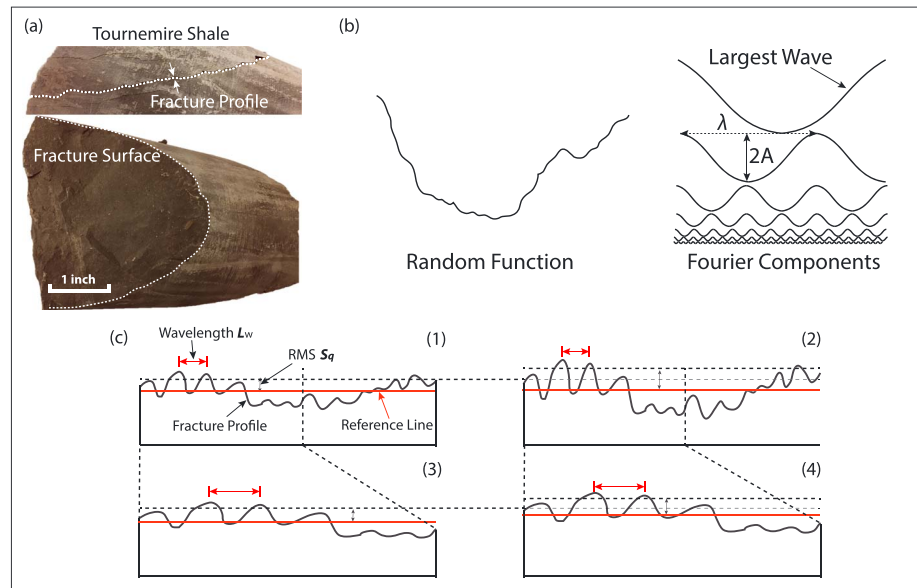


**Figure 1.** (a) Example of fracture surface of natural sedimentary rock (Tournemire shale) with fracture profile outlined by white curved dashed line. (b) The wavy surface profile may be represented as a random function decomposed as a Fourier series of sinusoidal components (modified from Brown, 1995). (c) Schematic graph of 1-D fracture profile showing scenarios of different combinations of asperity height  $S_q$  (i.e., the amplitude of an asperity from a reference plane) and asperity wavelength  $L_w$ : (c1 versus c2) same wavelength but different asperity height; (c1 versus c3) same asperity height but different wavelength; (c1 versus c4): different wavelength and different asperity height.

## 2. Experimental Methods

From the foregoing, we first examine the features of natural shale fractures. Then we create artificial fracture surfaces (as analogues to natural fractures), with controlled roughness features. Finally, we perform fracture shearing and fluid flow experiments with the artificial samples.

### 2.1. Characterization of Surface Roughness

A number of shear experiments have been performed on fracture surfaces with asperities that have predefined size and shape, for example, triangular sawtooth and sinusoidal asperities (Asadi et al., 2013; Huang et al., 2002; Pereira & De Freitas, 1993). However, these simple asperity shapes lack the characteristics of real rough surfaces, such as stochastic amplitude and wavelength. With observation of natural preexisting fractures (Figure 1a), the surface features can be described by the roughness—the characteristic deviation of the surface from a smooth plane. A typical mathematical model of a rough fracture surface suggests three key parameters: (1) the root-mean-square (RMS) roughness at a reference length scale, (2) a length scale describing the degree of mismatch, and (3) the fractal dimension (Brown, 1995). The irregular profile of real fracture surface can be considered as an analogue to an integration of a series of sinusoidal components (Figure 1b), each of which may play a role in shaping the surface textures as well as in influencing the fracture frictional strength, stability, and permeability. To reduce the complexity, we make a simplification by focusing on the role of the largest wavelength of fracture surface.

Hence, in this work, we assume that a fracture surface can be simply characterized by a combination of two geometric parameters (Figure 1c): (1) wavelength  $L_w$ , known as the distance between two statistical independent points on a fracture surface, and (2) the RMS asperity height ( $S_q$ ), which is also defined as the RMS values of roughness amplitude sampled in the area  $A$  as (Gadelmawla et al., 2002):

$$S_q = \sqrt{\frac{1}{A} \iint_A z(x, y) dx dy} \quad (5)$$

In addition to wavelength and RMS parameters, the physical features (e.g., asymmetry and flatness) of the surface roughness model can also be characterized by the surface geometry parameters: skewness ( $S_{sk}$ ) and kurtosis ( $S_{ku}$ ), which are introduced in the appendix.

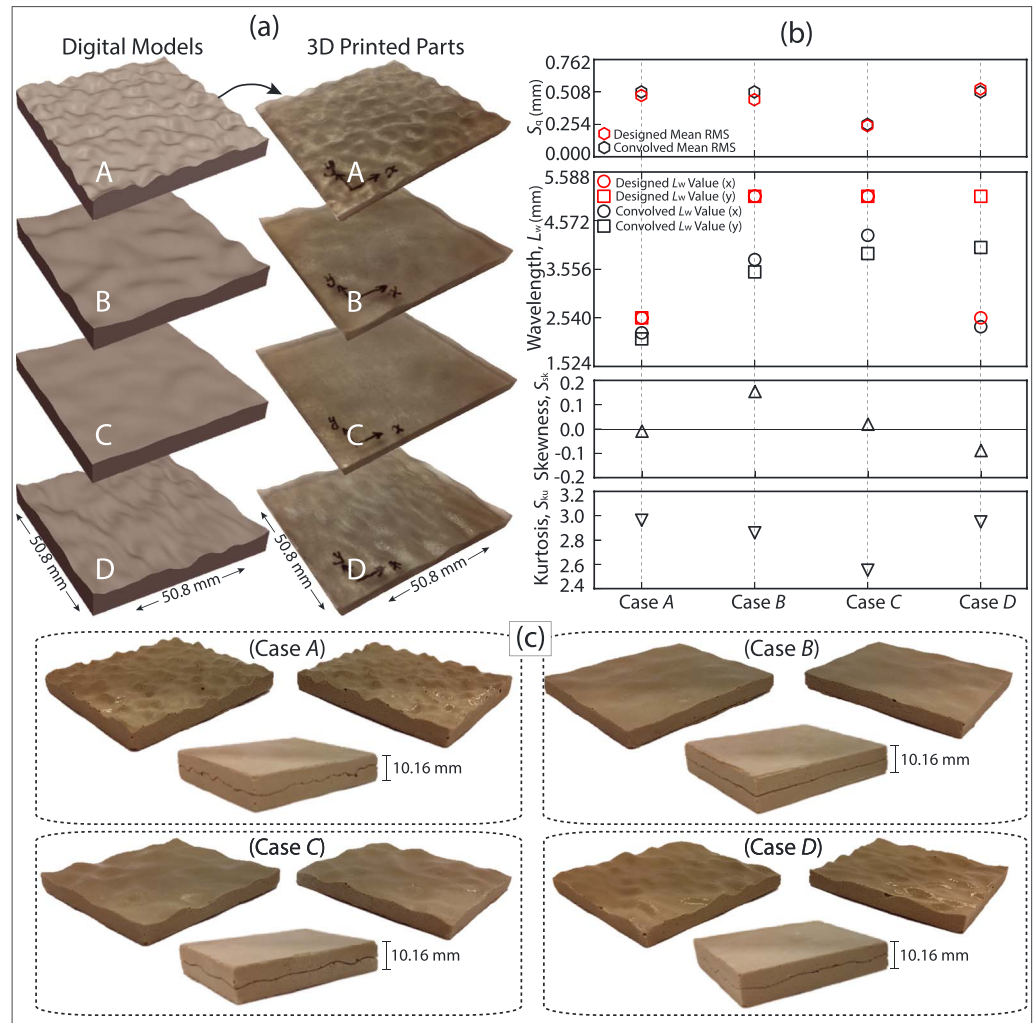


**Figure 2.** (a, left column) Fabricated digital fracture surface models and (right column) their 3-D printed counterparts. (b) Statistical roughness parameters of modeled surface geometry: root-mean-square height of asperity, wavelength, surface skewness, and surface kurtosis of surface geometry. The red symbols are design values, serving as reference values in generating the digital geometries of the fractures. The black symbols are the statistical characteristics based on the given reference values (red symbols). (c) Artificial fractures are cast with cemented calcite. The net thickness of the mated fractures is 10.16 mm (0.4 inch), and the horizontal dimension of each direction is 50.8 mm (2 inches).

## 2.2. Preparation of Artificial Samples With Controlled Roughness

A random roughness with Gaussian statistics is a well-accepted approximation of many real rough surfaces. We first make an uncorrelated Gaussian distribution of random roughness height  $S_q$ , and then generate the Gaussian-correlated profile  $z_u(x, y)$  convolved by a Gaussian filter (Fung et al., 2010). The designed 3-D digital

**Table 1**  
Statistical Roughness Parameters of Fracture Surface

Case no.	$S_q$ [mm]	$L_w^d(x)$ [mm]	$L_w^d(y)$ [mm]	$L_w^c(x)$ [mm]	$L_w^c(y)$ [mm]	$S_{sk}$ [–]	$S_{ku}$ [–]	$\bar{x}(S_q)$ [mm]	$s$ [mm]
(A)	0.508	2.54	2.54	2.2276	2.1006	–0.0089	2.9625	0.4801	–0.0025
(B)	0.508	5.08	5.08	3.7567	3.5001	0.1543	2.8592	0.4470	0.1168
(C)	0.254	5.08	5.08	4.2647	3.8837	0.0196	2.5517	0.2438	–0.0762
(D)	0.508	2.54	5.08	2.3546	4.0107	–0.0886	2.9493	0.4597	–0.0711

Note.  $L_w^d(x)$  and  $L_w^d(y)$  are the designed wavelength, and  $L_w^c(x)$  and  $L_w^c(y)$  are the convolved wavelength based on  $L_w^d(x)$  and  $L_w^d(y)$  values.  $\bar{x}(S_q)$  is the mean value of RMS asperity height;  $s$  is the standard deviation of RMS asperity height.

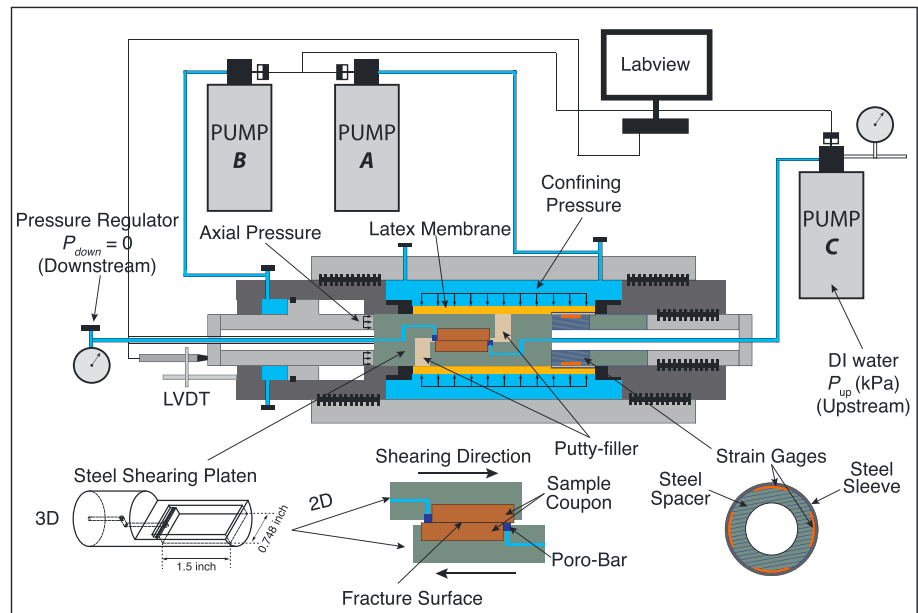


**Figure 3.** Schematics of experimental apparatus: Pump A (ISCO 500D) controls the confining stress applied on the fracture. Pump B (ISCO 500D) controls shear stress applied on the fracture. Pump C (ISCO 500D) outputs the fluid through fracture at a prescribed flow rate or pressure modified from Fang et al., (2018).

fracture surface geometries are illustrated in Figure 2a. The digital geometries have a resolution of 200 dpi (i.e., data points per inch) in each of the  $x$ ,  $y$ , and  $z$  directions. The statistical roughness parameters (i.e.,  $S_q$ ,  $L_w$ ,  $S_{sk}$ , and  $S_{ku}$ ) of surface geometry are shown in Figure 2b, where four cases are highlighted: (1) identical asperity height with different wavelength (i.e., Case A versus Case B), (2) identical wavelength with different asperity height (i.e., Case B versus Case C), (3) different wavelength with different asperity height (i.e., Case A versus Case C), and (4) identical asperity height and wavelength but sheared in two different directions (i.e., Case A versus Case D or Case B versus Case D). The values of surface roughness parameters are listed in Table 1.

From a physical interpretation, the highest positive skewness value ( $S_{sk} = 0.1543$ ) suggests the fracture (B) with the smoothest surface. The negative skewness values of surfaces (A) and (D) indicate the presence of comparatively few peaks on the fracture surfaces. Additionally, the kurtosis values of fractures (A) and (D) are relatively higher than those of fractures (B) and (C), suggesting that fractures (A) and (D) have sharper asperities than those of fractures (B) and (C). These features define the 3-D geometries of Figure 2a. Mechanically, when two well-mated rough surfaces slide against each other under a defined normal stress,

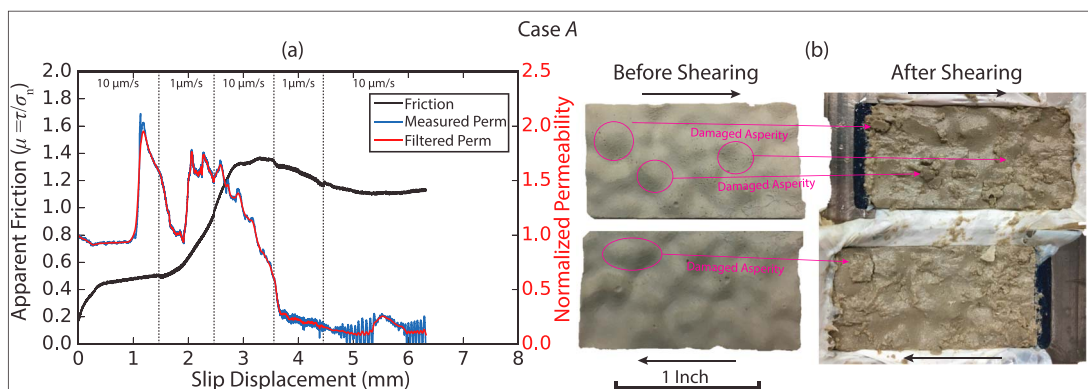


**Figure 4.** (a) Net frictional strength and permeability evolution with displacement for sample A. (b) Fracture surfaces before and after shear slip. The dimension of the matched fractures before slip is 37.186 mm × 18.644 mm × 10.897 mm (length × width × thickness).

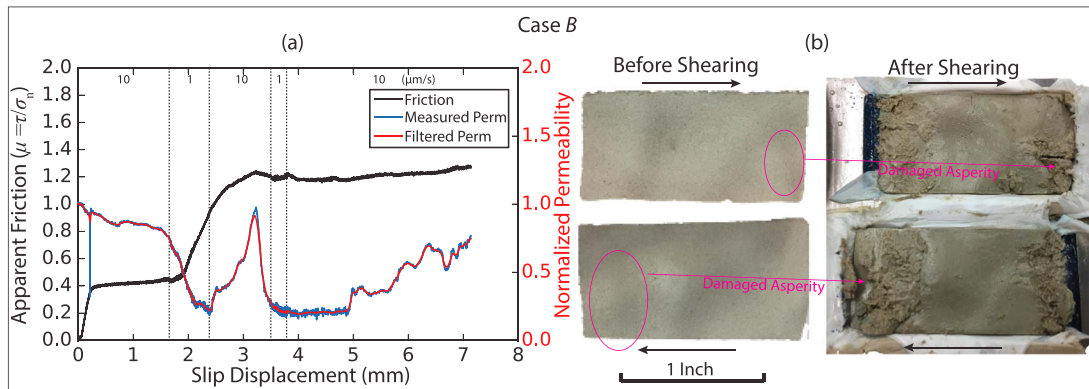


**Figure 5.** (a) Net frictional strength and permeability evolution with displacement for sample B. (b) Fracture surfaces before and after shear slip. The dimension of the matched fractures before slip is 37.059 mm × 18.517 mm × 11.049 mm (length × width × thickness).

the asperities may deform, fail, compact, or dilate to accommodate the motion. This requires an elastic strain on the order of the ratio of asperity height and length (Brodsky et al., 2016). With this definition, we define an analogous integrated roughness term  $R$  by applying the ratio of RMS height  $S_q$  and wavelength  $L_w$  (i.e.,  $R = S_q/L_w$ ), which statistically integrates the contributions from all of the asperities on the fracture surfaces. As implied from Brodsky et al. (2016), a higher  $S_q/L_w$  ratio may suggest that a larger elastic strain is required to accommodate the surface deformation until plastic failure and truncation of the asperities are induced. Given the parameters in Table 1, the calculated integrated roughness ratios of these samples are expressed as:  $R_a > R_d > R_b > R_c$ .

With these 3-D digital geometries (Figure 2a, left column), we apply 3-D printing to create (Figure 2a, right column) female resin molds for casting the artificial fracture samples. To print fine precision solid parts that can best represent the prescribed digital geometries, we specifically use Object260 Connex3 (Stratasys Ltd) instead of the most common jetting-polymer-drop method. Object260 Connex3 jet microscopic layers of liquid photopolymer onto a build tray that cures instantly from ultraviolet light. In printing the solid parts, we use digital material RGD875 (acrylic components) and select a high-quality build mode. The resolution of the printer is 600 dpi in the X direction, 600 dpi in the Y direction, and 1,600 dpi in the Z direction. The resolution of the printed parts is ~43  $\mu\text{m}$  horizontally and ~16  $\mu\text{m}$  vertically. The 3-D printing resolution is higher than that of the digital model, which suggests that the designed microfeatures of the fracture models can be fully duplicated in the printed counterparts. In fabricating artificial samples comprising natural minerals, we use the printed solid parts to create a resin mold. We then sieve the calcite powder and cement powder (Rapid Set® Hydraulic Cement) with particle sizes less than 106  $\mu\text{m}$  and uniformly mixed 37.5 wt % calcite and 37.5 wt % cements with 25 wt % DI water. The slurry is eventually cast in the resin mold for 3 days.

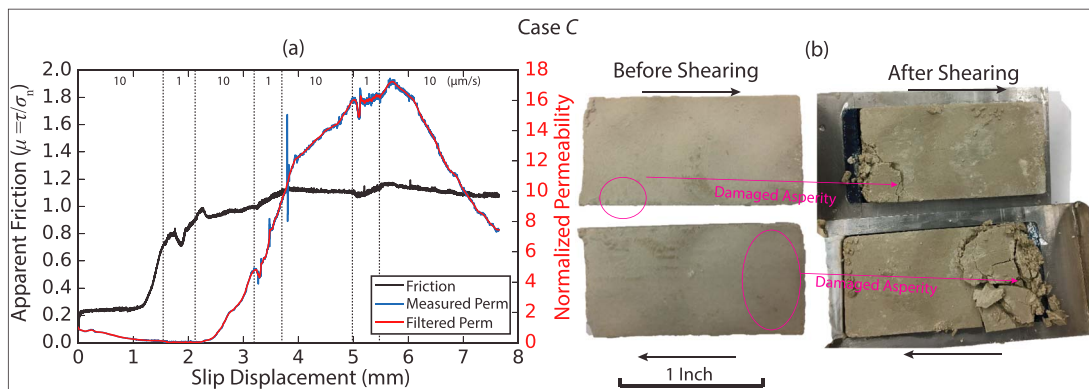


**Figure 6.** (a) Net frictional strength and permeability evolution with displacement for sample C. (b) Fracture surfaces before and after shear slip. The dimension of the matched fractures before slip is 37.109 mm × 18.440 mm × 11.100 mm (length × width × thickness).

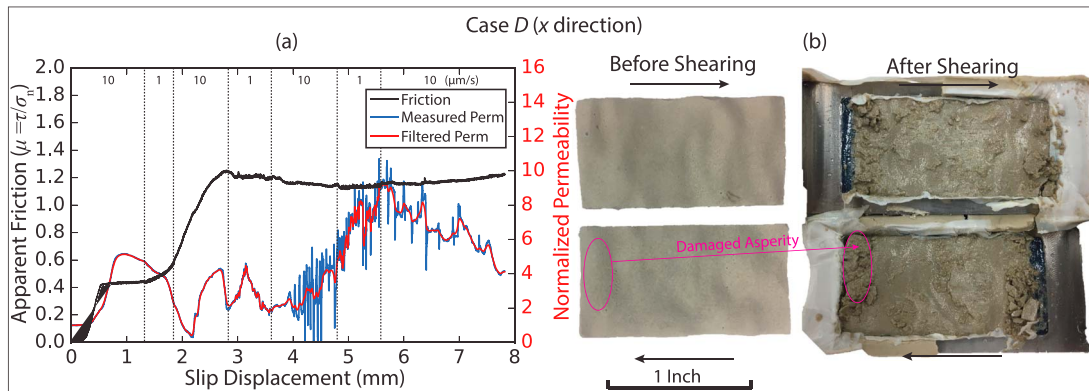


**Figure 7.** (a) Net frictional strength and permeability evolution with displacement for sample *D*. The shear direction is along *x* direction of sample *D* indicated in Figure 2a. (right) Fracture surfaces before and after shear slip. The dimension of the matched fractures before slip is 37.211 mm × 18.872 mm × 11.354 mm (length × width × thickness).

The artificial rock-like fracture samples are presented in Figure 2c. To provide control for the experimental results, we cast an artificial fracture (Case *E*) with a saw-cut planar surface. The fracture surface is uniformly polished with grinding powder (#60 grit carbide), and the heights of the asperities are at least 2 orders of magnitude smaller than those of fracture cases *A* to *D*.

### 2.3. Experimental Setup and Procedure

Friction-permeability experiments are performed in a modified triaxial testing apparatus (Temco) that individually applies confining stress and differential (end-to-end) pore pressure while the sample is sheared at a prescribed velocity (Figure 3). This allows the concurrent measurement of the evolution of fracture permeability and friction coefficient during shear slip. The sample coupons (fracture surfaces) are packed within a pair of steel shearing platens. The initial offset of platens is ~8 mm to accommodate slip displacement during sliding. The platen-offset gap is filled with putty-filler to prevent fluid short-circuiting. The side and bottom contacts between the sample coupon and the platen surfaces are covered with Teflon to prevent the leakage of the injected fluid that is presumed to migrate only along the fracture surfaces. The assembled platens are packed within a membrane to isolate the sample from the confining fluid. A steel sleeve covers the load cell to prevent it from being affected by the applied confining pressure.

To be consistent with the applied stress conditions of previous experimental studies (Fang et al., 2017, 2018), we apply a confining stress (normal stress) of 3 MPa dynamically controlled by pump A. Axial shear deformation progresses at constant rate, and is controlled by the stepped constant flow rates from pump B. The shear force is measured by the load cell. Meanwhile, we set a constant upstream fluid pressure of 120 kPa and

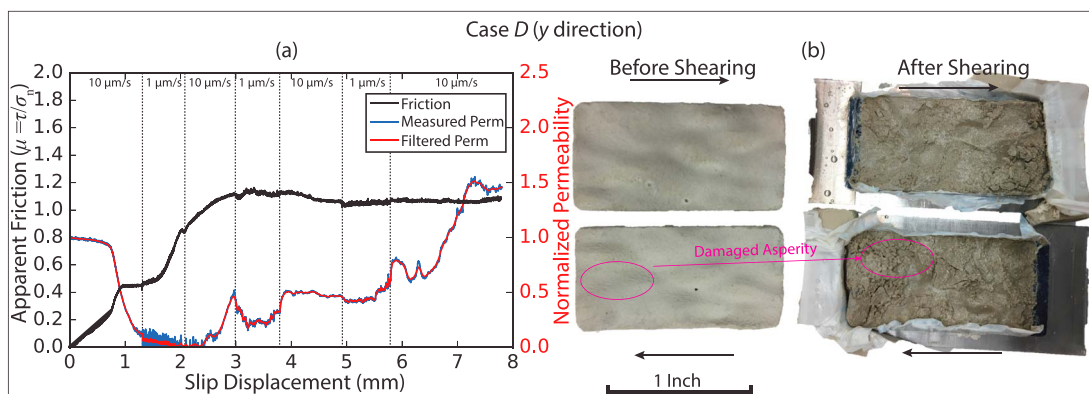


**Figure 8.** (a) Net frictional strength and permeability evolution with displacement for sample *D*. The shear direction is along *y* direction of sample *D* indicated in Figure 2a. (b) Fracture surfaces before and after shear slip. The dimension of the matched fractures before slip is 37.287 mm × 18.364 mm × 11.846 mm (length × width × thickness).

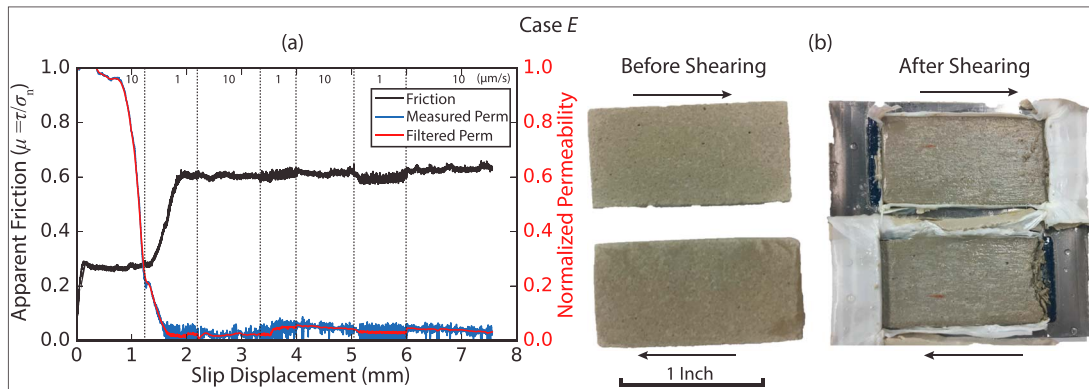


**Figure 9.** (a) Net frictional strength and permeability evolution with displacement for sample *E*. (b) Fracture surfaces before and after shear slip. The dimension of the matched fractures before slip is 37.033 mm × 18.313 mm × 11.913 mm (length × width × thickness).

measure its flow rate with pump C. The minimum flow rate of each pump is 0.001 ml/min, and the display resolution of the pump pressure transducer is 1.0 kPa. A load cell with a resolution of 0.3 kPa is used to measure the axial stress. At room temperature, the minimum measurable permeability is  $1.0 \times 10^{-14} \text{ m}^2$ .

We conduct velocity-stepping experiments to compare the frictional, stability, and permeability response to varying velocities for six different scenarios: cases *A*, *B*, *C*, *D<sub>x</sub>*, *D<sub>y</sub>*, and *E*. It is worth noting that sample *D* has an anisotropic correlation length along the *x* and *y* directions; therefore, we run two experiments for sample *D*, one shearing along the *x* direction and the other shearing along the *y* direction. The shear velocity is set to 10 μm/s (monotonic) and switched by downsteps and upsteps between 1 and 10 μm/s, until a displacement of ~6 to 8 mm is reached. All the experiments are performed at room temperature (25 °C), with shear displacements recorded by linear variable differential transformer located outside the vessel.

### 3. Results and Discussions

We first introduce broad observations of concurrent friction, stability, and permeability evolution during shearing. Then, we explore how frictional strength, frictional stability, and permeability change are controlled by roughness variations of the fracture surface.

**Table 2**  
Measured Frictional and Permeability Parameters of Fracture Samples

Sample	$k_{ini}$ (m <sup>2</sup> )	Velocity step	$\tau/\sigma_n$	( <i>a</i> - <i>b</i> )	$u_s$ (mm)	$D_c$ (μm)	$\Delta u^i$	$k_0^j$	$\Delta k^j$
rg_A	2.1335E-11	1	0.89	0.0009	2.46	90	0.4860	1.5398	0.1713
		2	1.176	-0.0002	4.46	40	0.4290	0.1565	0.0029
rg_B	1.53E-12	1	0.576	0.0003	2.12	15	0.2860	0.2795	0.0898
		2	1.186	-0.0024	3.79	50	0.4990	0.2074	0.0147
rg_C	7.42E-12	1	0.84	0.0007	2.15	80	0.0935	0.0144	0.0054
		2	1.061	-0.0004	3.7	50	0.1175	9.1366	0.0014
		3	1.115	-0.0008	5.5	50	0.2180	16.2394	0.8304
rg_D <sub>x</sub>	2.90E-12	1	0.542	0.0032	1.8	160	0.0175	2.2096	0.2027
		2	1.193	0.0012	3.61	100	0.5180	9.0353	-1.1298
		3	1.135	0.0009	5.6	70	0.1825	1.7837	0.4963
rg_D <sub>y</sub>	3.45E-12	1	0.628	0.0011	1.89	120	0.0775	0.0044	0.0085
		2	1.08	0.0007	3.78	35	0.2000	0.3245	0.1729
		3	1.056	0.0004	5.8	40	0.0350	0.5604	0.2258
rg_E	1.23E-11	1	0.6	-0.0004	2.2	30	0.2995	0.0232	0.0078
		2	0.61	-0.0005	4	45	0.4990	0.0445	0.0112
		3	0.595	-0.001	5.9	50	0.4055	0.0299	0.0115

Note. All samples are sheared at an effective normal stress of 3 MPa. The frictional stability data points are obtained at each velocity step from 1 to 10 μm/s.

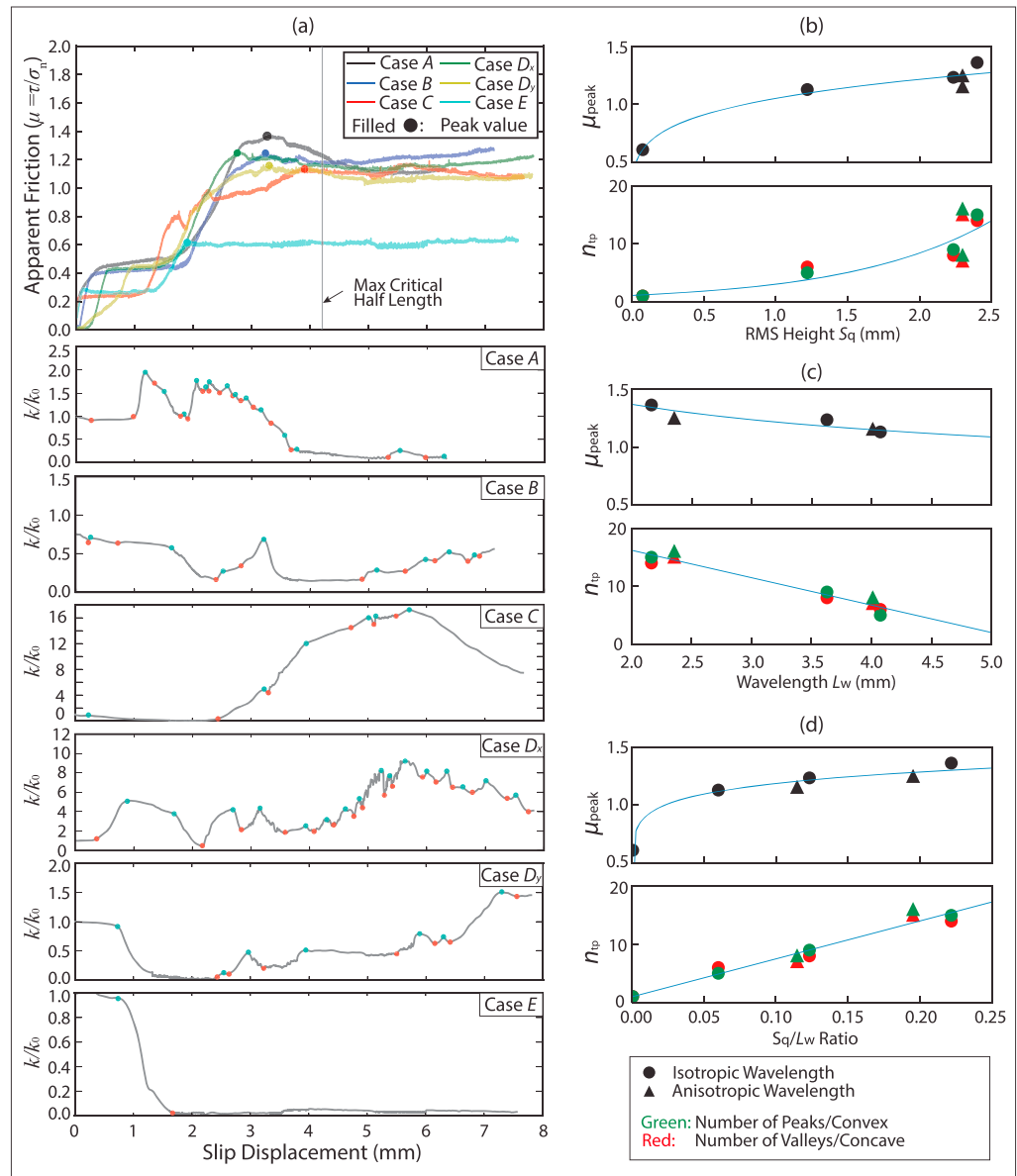


**Figure 10.** (a) Friction-displacement curves of samples under an effective normal stress of 3 MPa. A yield point (peak point) is labeled before a displacement of half the critical wavelength; (b) effect of RMS height  $S_q$ , (c) effect of wavelength  $L_w$ , and (d) effect of  $S_q/L_w$  ratio.

### 3.1. Net Friction and Permeability Evolution

The frictional strength is calculated by the ratio of measured shear stress and the effective normal stress as  $\mu = \tau/\sigma_n$ . Given the assumption that the apertures of rough fractures are averaged over two parallel planar surfaces, the equivalent fracture permeability is calculated using the cubic law as

$$e_h = - \left( \frac{12\mu_{vis} \cdot L(t) \cdot Q(t)}{W \cdot \Delta P_f} \right)^{1/3} \quad (6)$$

$$k = \frac{e_h^2}{12} \quad (7)$$

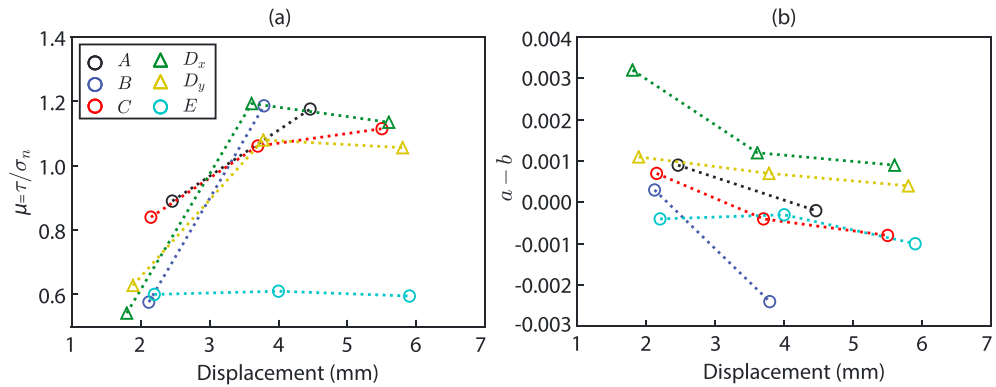


**Figure 11.** (a) The apparent frictional strength; (b) the frictional stability values at the displacement where up-velocity steps are applied.

where  $e_h$  [m] is the equivalent hydraulic aperture,  $\mu_{vis}$  [Pa·s] is the viscosity of fluid,  $L(t)$  [m] is the contact length of the fracture surface,  $W$  [m] is the fracture width,  $Q(t)$  [m<sup>3</sup>/s] is the measured flow rate, and  $\Delta P_f$  [Pa] is the differential fluid pressure between the upstream and downstream extent of the fracture.

Results of net friction and permeability evolution with displacement on samples A to E and the corresponding images of fracture surfaces before and after the shear slip are individually shown in Figures 4–9. The measured permeability data, as plotted in blue, are processed by Butterworth filter (filter order = 1, cutoff frequency = 0.01). In each case, the dimensionless permeability is plotted, which is defined as the measured permeability normalized to the initial static permeability value  $k_{ini}$  before shearing (Table 2).

All friction curves with displacement are compared in Figure 10a. All samples show similar initial frictional strength within a slip range of ~1 to 1.5 mm, which is mainly due to a slight mismatch between the actual sample length (i.e., ~37.033 to 37.287 mm) and the length of the shear platen inner cell (i.e., 38.1 mm in Figure 3). For samples with large asperities, their friction evolution shares similar general trends, all ending with a magnitude greater than 1—likely due to the effect of interlocking asperities. Accordingly, permeability of samples A to D during shearing alternately increases and decreases as a result of combined effects of dilation, compaction or clogging. By contrast, the frictional strength of sample E presents a much lower evolution profile as a result of low roughness of the fracture surface. The permeability of sample E monotonically declines with displacement due to the continuing produced wear products filling and clogging the fracture aperture (Fang et al., 2017).

The contrast between presheared and postsheared samples, as imaged in Figures 4–9 indicates that surface asperities are sheared-off during reactivation and the wear products relocate and remain within the topographically modified aperture. The evolving effects of contact junction size on flow paths are best reflected in

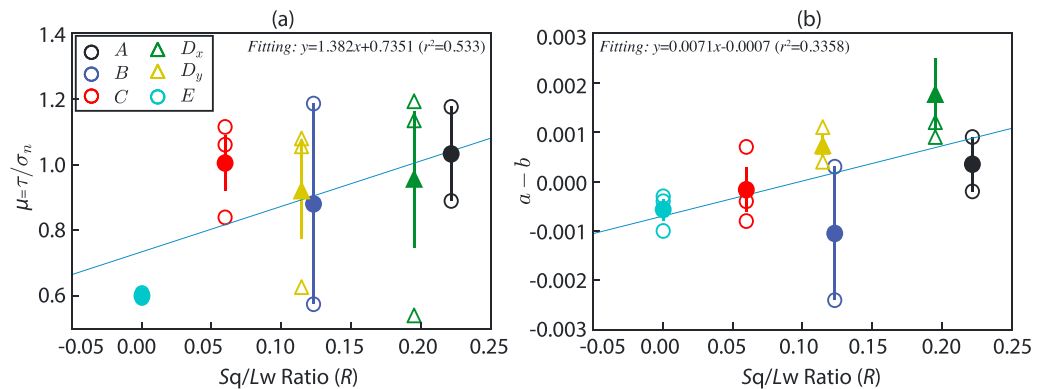


**Figure 12.** (a) Correlation of apparent frictional strength (i.e., shear stress-normal stress ratio) and  $Sq/L_w$  ratio; (b) correlation of frictional stability values and  $Sq/L_w$  ratio. The filled symbols refer to the mean values defined by the unfilled symbols.

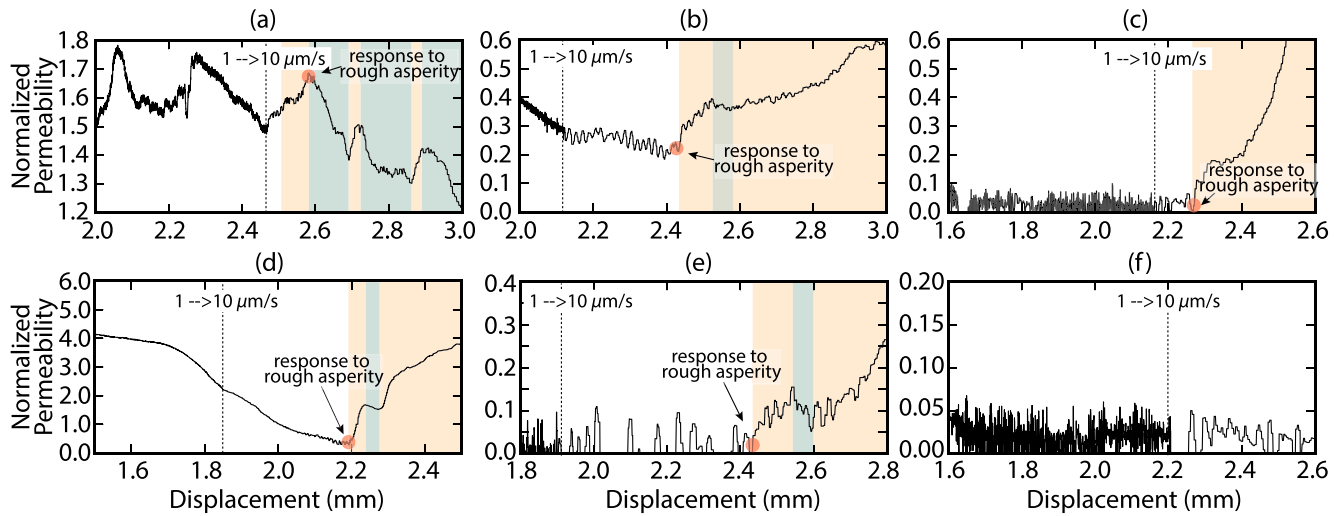


**Figure 13.** Permeability evolution with the effect of higher amplitude (rouger) asperities: (a) Sample A, (b) Sample B, (c) Sample C, (d) Sample  $D_x$ , (e) Sample  $D_y$ , and (f) Sample E. The red shading highlights the permeability change due to the velocity step, while the yellow and blue shading highlight the dilation and compaction due to rough asperities.

the net permeability data, while the clogging behavior may be overlooked by merely measuring the normal dilation displacement.

In addition to the distinct surface roughness pattern, the direction of shear slip with respect to surface roughness direction may severely influence the permeability evolution history. Samples  $D_x$  and  $D_y$ , with identical asperity height and wavelength, are sheared in two different directions, showing that the highest dimensionless permeability of sample shear in the direction perpendicular to its larger wavelength is approximately (Figure 7) ~6 to ~7 times larger than that sheared in the direction parallel to its larger wavelength (Figure 8).

To explore the relationship between friction and surface roughness, we define two parameters: (1) *apparent coefficient of friction at peak* ( $\mu_{peak}$ ) as the frictional yield value at a slip displacement less than the wavelength of a fracture and (2) *number of permeability inflection points* ( $n_i$ ) as the number of peaks or valleys where

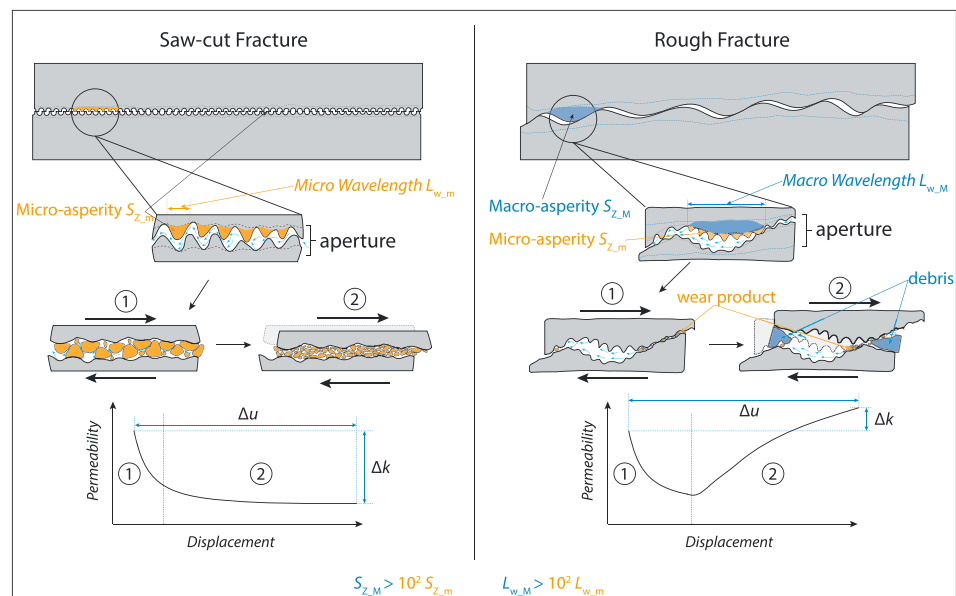


**Figure 14.** Schematic diagram shows concepts of micro/macro asperity ( $S_{z,m}/S_{z,M}$ ) and micro/macro wavelength ( $L_{w,m}/L_{w,M}$ ) of a saw-cut (smooth) fracture and a rough fracture.

permeability changes from an uptrend to a downtrend or from a downtrend to an uptrend, during shearing. These inflection points are located by taking the discrete derivative with a sampling rate of 0.1 Hz of the smoothed permeability data followed by filtering out unqualified data points. The inflection points are highlighted in Figure 10a for clarity.

A strong correlation between the aforementioned two parameters (i.e.,  $\mu_{\text{peak}}$  and  $n_i$ ) and RMS height ( $S_q$ ) and wavelength ( $L_w$ ) is observed in Figures 10b and 10c, representing that the peak frictional strength ( $\mu_{\text{peak}}$ ) and the number of permeability inflection point ( $n_i$ ) respectively decrease with wavelength but increases with both RMS height ( $S_q$ ) and the  $S_q/L_w$  ratio. This is because (1) mechanically, a fracture with a higher  $S_q/L_w$  ratio demands a larger elastic deformation and requires larger shear stress to fail the asperity for fracture surface accommodation (Brodsky et al., 2016), and (2) hydraulically, a higher  $S_q/L_w$  ratio leads to more cycles of dilation and compaction during shearing. However, weak correlations are found between parameters ( $\mu_{\text{peak}}$  and  $n_i$ ) and surface features (i.e., skewness and kurtosis), which are illustrated in Figure A1 in the Appendix.

### 3.2. Friction Parameters and Permeability Change

For hydraulic rate-and-state friction experiments performed on fabricated samples, we determine the frictional parameters (i.e., apparent frictional strength  $\mu = \tau/\sigma_n$  and stability [ $a-b$ ]) by fitting experimental and modeled data via equations (2) and (3). The zoomed-in views of friction and permeability responses are shown in Figures A2, A3, A4, A5, A6, A7. The evolution of the frictional strength and stability with shear displacement is shown in Figure 11. Comparison of the constitutive frictional parameters for both rough and smooth surfaces indicates several significant results: First, the friction results as a whole indicate significant difference between the rough (samples A to D) and smooth surface (sample E). In Figure 11a, rougher fractures indicate greater slip hardening from  $\sim 2$  to 4 mm, then the effect of slip hardening deteriorates to a minimum level after a slip of  $\sim 4$  mm, implying that the interlocked large asperities may have mechanically failed within a slip displacement of one wavelength (Figure 10a). Rougher surfaces (samples A to D) also present higher frictional stability during initial slip comparing to that of a smooth surface (sample E; Figure 11b). The frictional stability ( $a-b$ ) of rough and smooth surfaces slightly decreases with increasing displacement. However, whether this observation extends to greater net displacement (e.g.,  $> 10$  mm) remains to be examined. In the frame of rate-and-state friction theory, this degradation of frictional stability ( $a-b$  values) suggests that the velocity strengthening properties of fractures (i.e., fractures sliding aseismically or stably) can evolve to velocity weakening (i.e., a necessary condition for fractures to fail seismically or unstably) with shear slip.

Figure 12 shows that both apparent frictional strength and stability increase with the roughness ratio, implying that fractures with low roughness are prone to reactivation and are more likely to fail seismically. This result is consistent with previous experimental work that shows effects of roughness on fracture frictional behaviors in response to wear and gouge formation (Marone & Cox, 1994). In addition to this, the roughness-frictional stability relationship from our experiments agrees well with the suggested frictional stability regimes from Harbord et al. (2017) that with normal stresses below 30 MPa, the frictional stability increases with roughness. In contrast, these frictional parameters do not show conspicuous dependence on skewness and kurtosis, which is reported in Figure A8.

It should also be noted that, though samples tested in cases  $D_x$  and  $D_y$  show identical asperity height and wavelength (i.e., both are from sample D in Figure 2), the frictional parameters differ when slip direction relative to its fracture asperity orientation is different (i.e., case  $D_x$ —slip in  $x$  direction versus case  $D_y$ —slip in  $y$  direction). In Figures 11 and 12, case  $D_x$  shows higher apparent frictional strength and stability than  $D_y$ , mainly because the wavelength is smaller in the  $x$  direction than in the  $y$  direction, resulting in a higher  $S_q/L_w$  ratio for case  $D_x$ .

In the above shear experiments, the measured apparent frictional strength of a fracture surface is an upscaled feature, which integrates the average influence of each individual asperity on a fracture surface. The laboratory-scale experimental results imply that the first reactivation of a rough fracture or fault may not occur due to the cohesive interlocking effect while a seismic event is more likely to nucleate on a fracture or fault with a smoother surface due to the low frictional strength and stability. This suggestion aligns with crustal-scale field observations that natural fault shear strength increases with curvature and mega-earthquakes preferentially occur on smooth or flat interfaces (Bletery et al., 2016; Wang & Bilek, 2014). As implied in Figure 11b, when a rough fracture or fault has met the Coulomb-Mohr criterion is reactivated, it

may fail aseismically in its initial stage and evolve to seismic failure as shear strain accumulates. This may be supported by the in situ observation that seismicity can be triggered by the evolution of aseismic slip (Guglielmi et al., 2015).

Previously presented results indicate that net permeability evolution and the frictional parameters are controlled by the fracture roughness (Figures 4–12). In the following, we explore the direct relationship between frictional parameters and local transient permeability change in response to velocity steps. To compare the relative magnitude of the change in permeability, we first define a normalized permeability change term as

$$\frac{\Delta k^i}{k_0^i} = \frac{k_{\text{real}}^i - k_{\text{sim}}^i}{k_0^i} \quad (8)$$

where  $k_0^i$  is the reference permeability before the instantaneous step in shear velocity change,  $i$  refers to the  $i$ th velocity step, and  $\Delta k^i$  is the permeability difference between the measured permeability  $k_{\text{real}}^i$  and the assumed permeability without the velocity change  $k_{\text{sim}}^i$ .  $k_{\text{sim}}^i$  is the permeability calculated from the evolving fracture aperture  $e_{\text{h\_evo}}$  within a certain slip displacement  $\Delta U^i$ , under an assumed scenario of no velocity step. The evolving aperture  $e_{\text{h\_evo}}$  is empirically estimated by assuming a velocity-dependent compaction or dilation coefficient during shearing. The detailed method of estimating  $e_{\text{h\_evo}}$  can be found in Fang et al. (2017). Equation (8) describes the relative change in permeability with respect to the permeability at the point before velocity change. The above calculated parameters are listed in Table 2.

The correlations between permeability change and frictional parameters are shown in Figures A9a and A9b, indicating that  $\Delta k^i/k_0^i$  is independent of  $(\tau/\sigma_n)$  and  $(a-b)$ . Such lack of correlation or weak correlation between permeability change and frictional stability may only be due to a small variation of  $(a-b)$  values measured from the same materials. Most  $\Delta k^i/k_0^i$  values are close to zero, suggesting that for those fabricated samples, very small permeability change occurs after fractures experience an instantaneous step in shear velocity changes. The velocity step-induced permeability changes (i.e.,  $\Delta k^i/k_0^i$ ) with respect to fracture roughness  $S_q/L_w$  ratios are plotted in Figure A9c, showing an uncorrelated trend between transient permeability changes and fracture roughness  $S_q/L_w$  ratio. Such a disconnection between transient permeability changes and surface skewness and kurtosis is reported in Figure A10.

Comparing with previous fracture shearing and fluid flow experiments on smooth natural fractures, the net permeability evolution of smooth surfaces (sample *E* in Figure 9) shows a similar monotonically declining trend with displacement (Fang et al., 2017; Im et al., 2018; Wu et al., 2017). The permeability decrease is due to the production of wear products, although dilation is temporarily triggered by the instantaneous increase in shear velocity. For rougher surfaces, although instantaneous dilation due to sudden velocity change can be observed over a small displacement (Figures 13a–13e), the roughness effect significantly contributes to a distinct net permeability increase over the slip. This means that an instantaneous velocity change may only affect a small transient permeability increase over a small slip displacement immediately after a velocity up-step, while over a large displacement, the roughness is the major factor influencing the change in permeability.

From a microscopic point of view, the observed permeability evolution is associated with the fracture tortuosity and connectivity of fluid pathways. These vary with the fracture contact area and the shape of the aperture distribution (Tsang, 1984). Thus, we employ an empirical equation that correlates fracture permeability to fracture tortuosity and roughness, which is expressed as follows (Akhavan & Rajabipour, 2012; Marsily, 1986):

$$k = \frac{T \cdot e_h^2}{12 \cdot [1 + \zeta \cdot (S_q/e_h)^{1.5}]} = \frac{(L_{\text{ref}}/L_{\text{eff}})^2 \cdot e_h^2}{12 \cdot [1 + \zeta \cdot (S_q/e_h)^{1.5}]} \quad (9)$$

where  $k$  is the fracture permeability,  $T$  is the tortuosity factor (Bear, 1988),  $\zeta$  is an empirical constant coefficient,  $S_q$  is the RMS value of the fracture asperity height,  $L_{\text{ref}}$  is the length of the reference line, and  $L_{\text{eff}}$  is the effective length of the streamline of voids in the porous medium or the total length of the wavy fracture profile, which are illustrated in Figure 1c. For the case of an ideal smooth fracture with two parallel walls,  $T = (L_{\text{ref}}/L_{\text{eff}})^2$  is equal to 1 and  $S_q = 0$ , then equation (9) is identical to equation (7). We use

equation (9) to interpret two scenarios (Figure 14) summarized from our experimental observations of permeability evolution.

(1) A smooth fracture surface can be characterized by micro asperity height  $S_{z,m}$  and micro wavelength  $L_{w,m}$  (Figure 14a). Considering that these asperities of fracture surfaces play significant roles for maintaining void spaces or propping two facing fracture planes (Jaeger et al., 2007; Ishibashi et al., 2016), in the shearing process, destruction of these sinusoidal asperities smoothens the fracture walls (Fang et al., 2017) and generates granular wear products that are compacted between fracture walls. This primarily increases the total length of the in-plane flow path within the fracture aperture and reduces the tortuosity factor  $T$  in equation (9). Together with the mechanical compaction occurring during shear slip, the fracture permeability monotonically declines. This declining trend gradually vanishes when shear displacement is sufficiently large. The asperity height becomes constant, and the evolution of porosity of wear products reaches dynamic equilibrium (Wang et al., 2017).

(2) A rough fracture surface can be characterized by macro asperity height  $S_{z,M}$  and macro wavelength  $L_{w,M}$  (Figure 14b). For the case of a rougher surface, the microscale asperity features (i.e., height  $S_{z,m}$  and wavelength  $L_{w,m}$ ) can be identified on the macro asperity. When well-matched rough fracture walls begin to collide, the two surfaces compact and interlock during initial closure and fine-size granular wear products may be generated by shearing-off of the micro asperities. In this process, when the wear products (i.e., rock-forming minerals are broken down or crushed on the fracture surfaces) remain within the fracture and clog the flow pathways, the tortuosity factor  $T$  is reduced while the aperture  $e_n$  and  $S_q$  have not yet significantly changed. Thus, at this initial stage, the fracture permeability reduction is primarily due to the tortuosity effect. As the fracture surface continues to slide against each other, the asperity debris may promote a strong dilation and out-of-plane flow becomes dominant, leading to permeability enhancement (Figure 14b). However, while the residual asperities slide against each other and the wear products relocate and settle along the fracture walls, the fracture tortuosity factor  $T$ , fracture aperture  $e_n$ , as well as the relative roughness ratio ( $R = S_q/L_w$ ) evolve simultaneously. Considering all these variables, the permeability may increase, decrease, or remain unchanged during shearing. Above physical processes allow the interpretation of the initial permeability decrease and later observed compaction and dilative behaviors of fractures observed in Figures 4–9.

#### 4. Conclusions

Our fracture shearing and fluid flow experiments on a series of fabricated fracture surfaces with specified roughness features highlight the effect of fracture roughness on possible relationship between concurrent frictional behavior and permeability evolution.

Our experimental results show that (1) rougher surfaces exhibit more positive velocity-strengthening frictional behavior and higher frictional strength than that of smooth fracture due to the increased interlocking of asperities during shearing. This implies that rough fracture or fault may be difficult to be reactivated. (2) Both smooth and rough fracture surfaces exhibit velocity strengthening frictional behavior in the initial stage of shearing and their strengthening behaviors evolve to velocity neutral and velocity-weakening with displacement, suggesting an aseismic to seismic transition. (3) The roughness pattern has a significant control on permeability evolution over the entire shearing history. Permeability reduces monotonically for smooth fracture but evolves in a fluctuating pattern for significantly rough fractures. A higher roughness is likely to result in alternating compaction and dilation during shearing. Significant permeability enhancement is observed for rough samples, but serious permeability damage may also occur when asperities are highly damaged and truncated to block fluid pathways. (4) As experiments are performed on a single material, there is no conspicuous correlation between local transient permeability evolution and local frictional behavior (i.e., frictional strength and stability) for rough fracture samples when fractures subject to sudden sliding-velocity change.

#### Appendix A

Skewness is expressed as the ratio of the mean of the cube of height values and the cube of  $S_q$  within a sampling area  $A$ ,

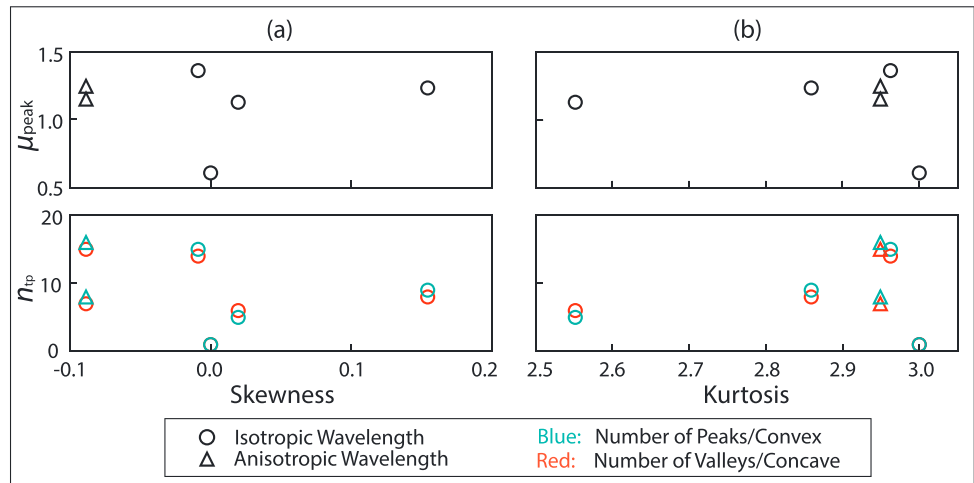


Figure A1. (a) Relationship of skewness and  $\mu_{peak}$  and  $n_{ip}$ ; (b) relationship of kurtosis and  $\mu_{peak}$  and  $n_{ip}$ .

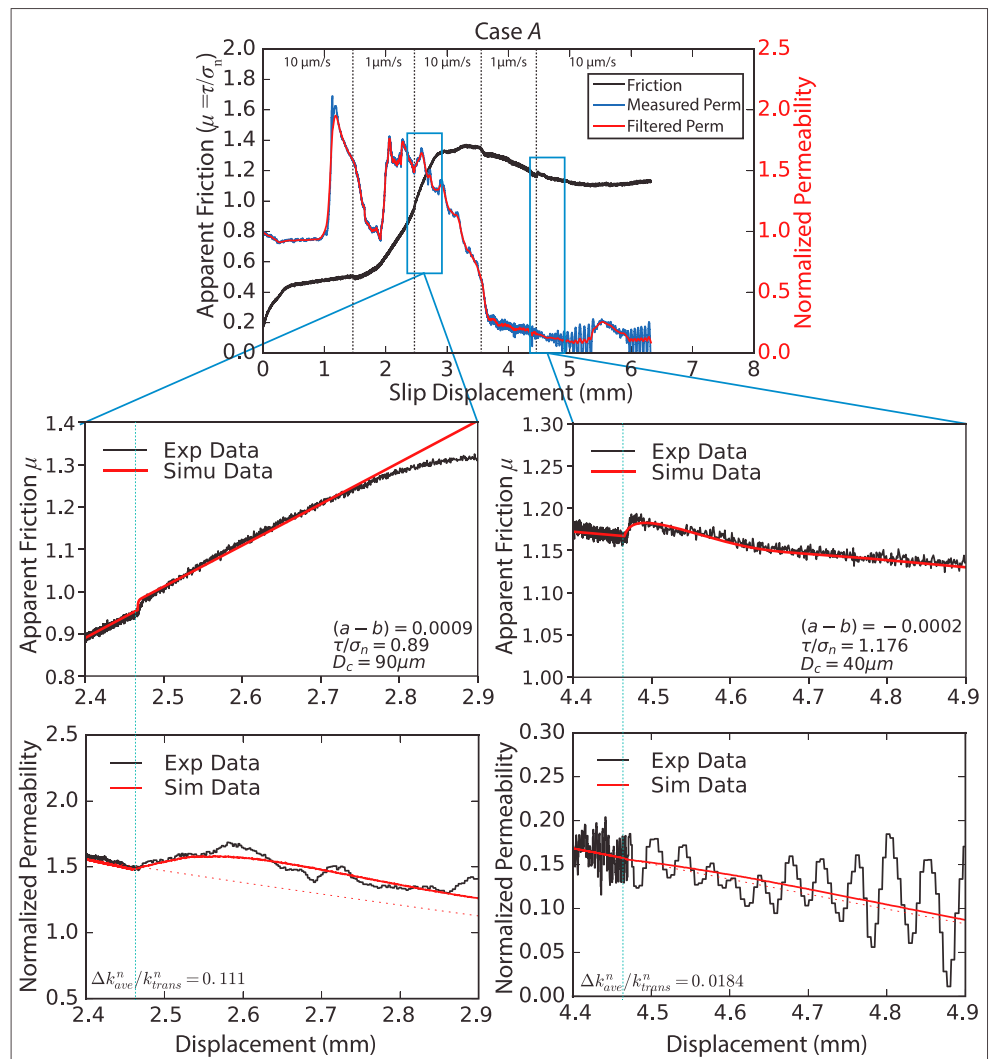
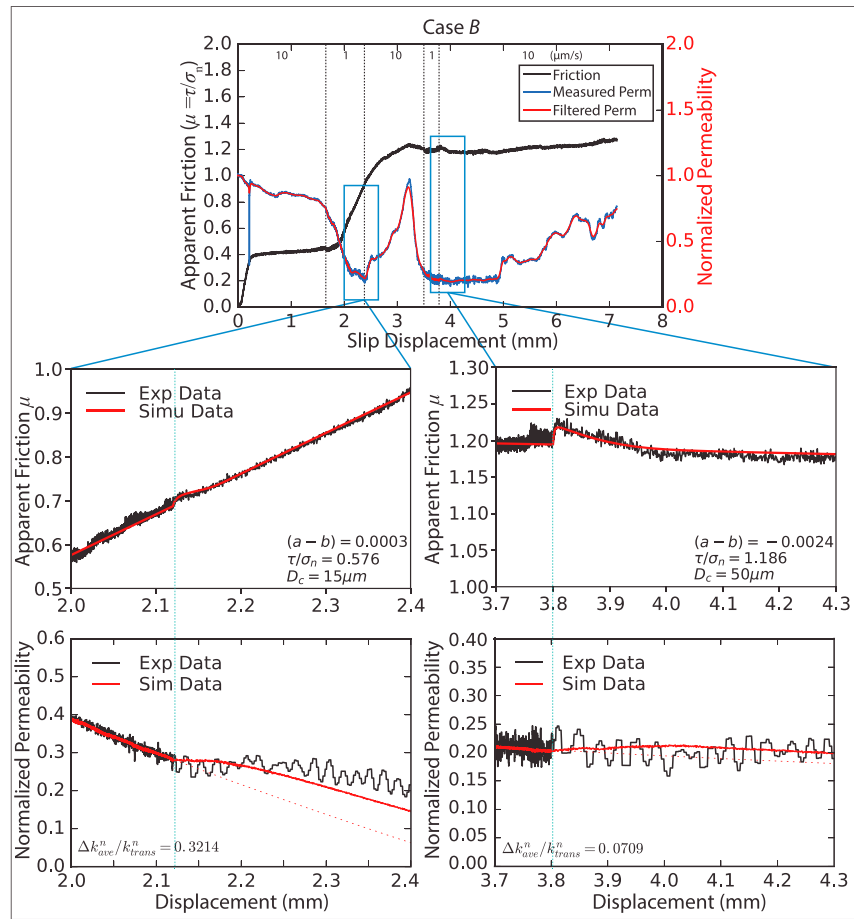
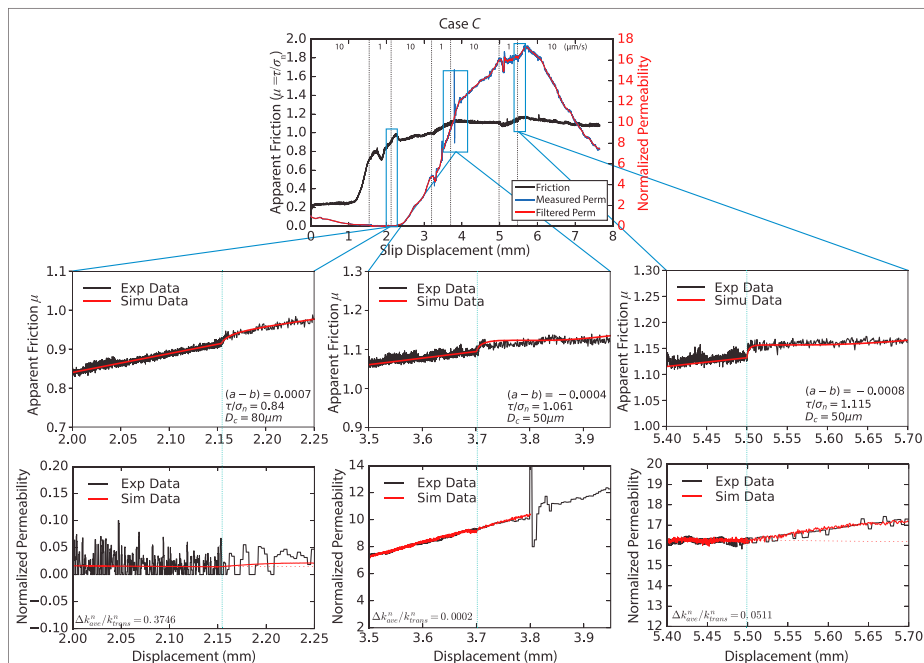


Figure A2. Friction-permeability data for fracture surface A. In each case data represent the friction response to an up-velocity step change in load point velocity.



**Figure A3.** Friction-permeability data for fracture surface B. In each case data represent the friction response to an up-velocity step change in load point velocity.



**Figure A4.** Friction-permeability data for fracture surface C. In each case data represent the friction response to an up-velocity step change in load point velocity.

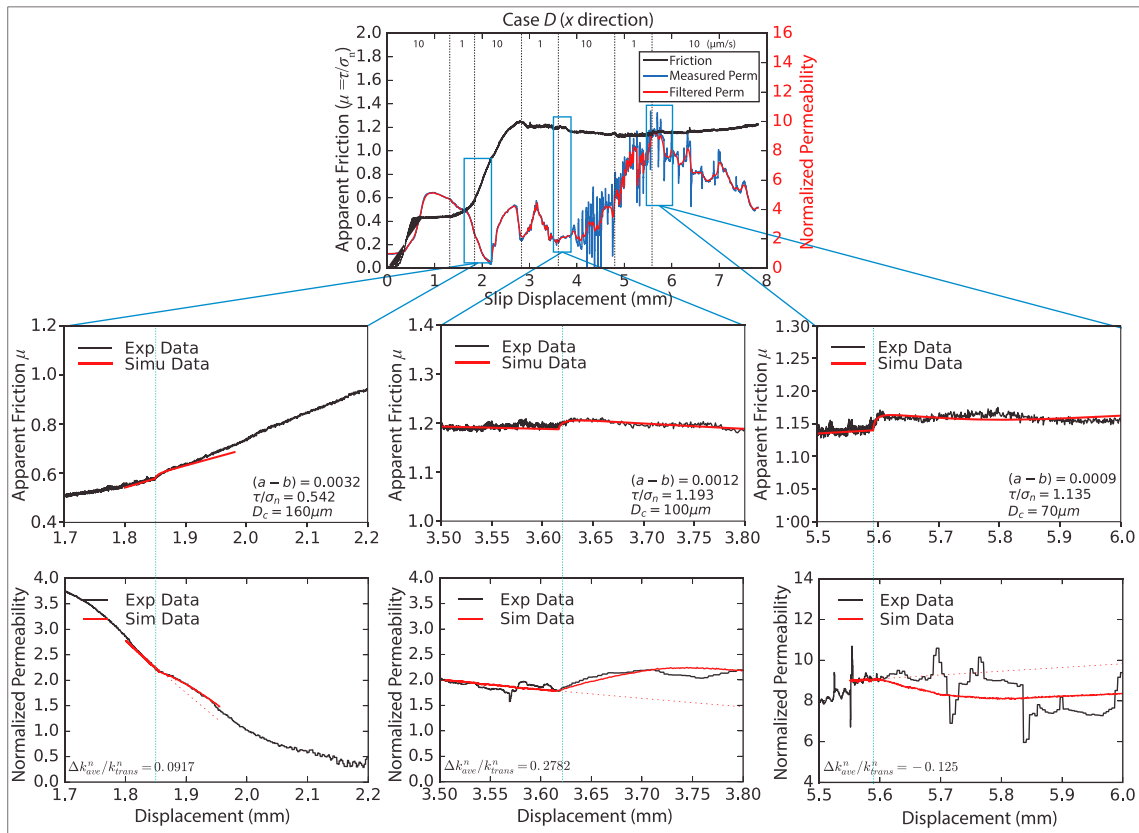


Figure A5. Friction-permeability data for fracture surface  $D_x$ . In each case data represent the friction response to an up-velocity step change in load point velocity.

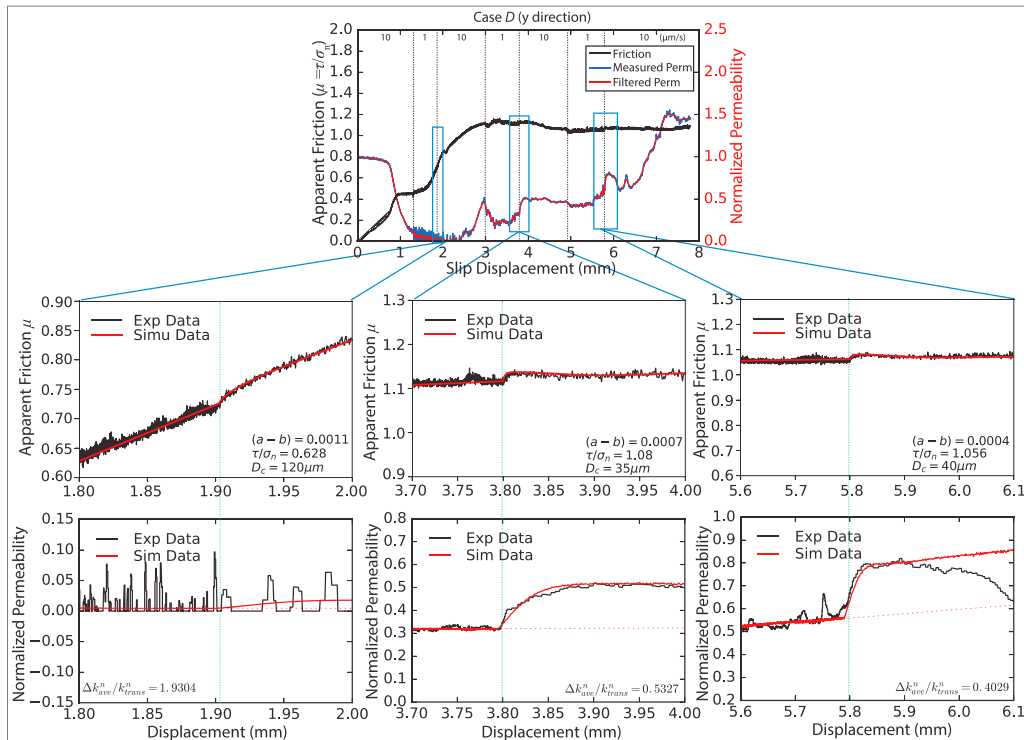
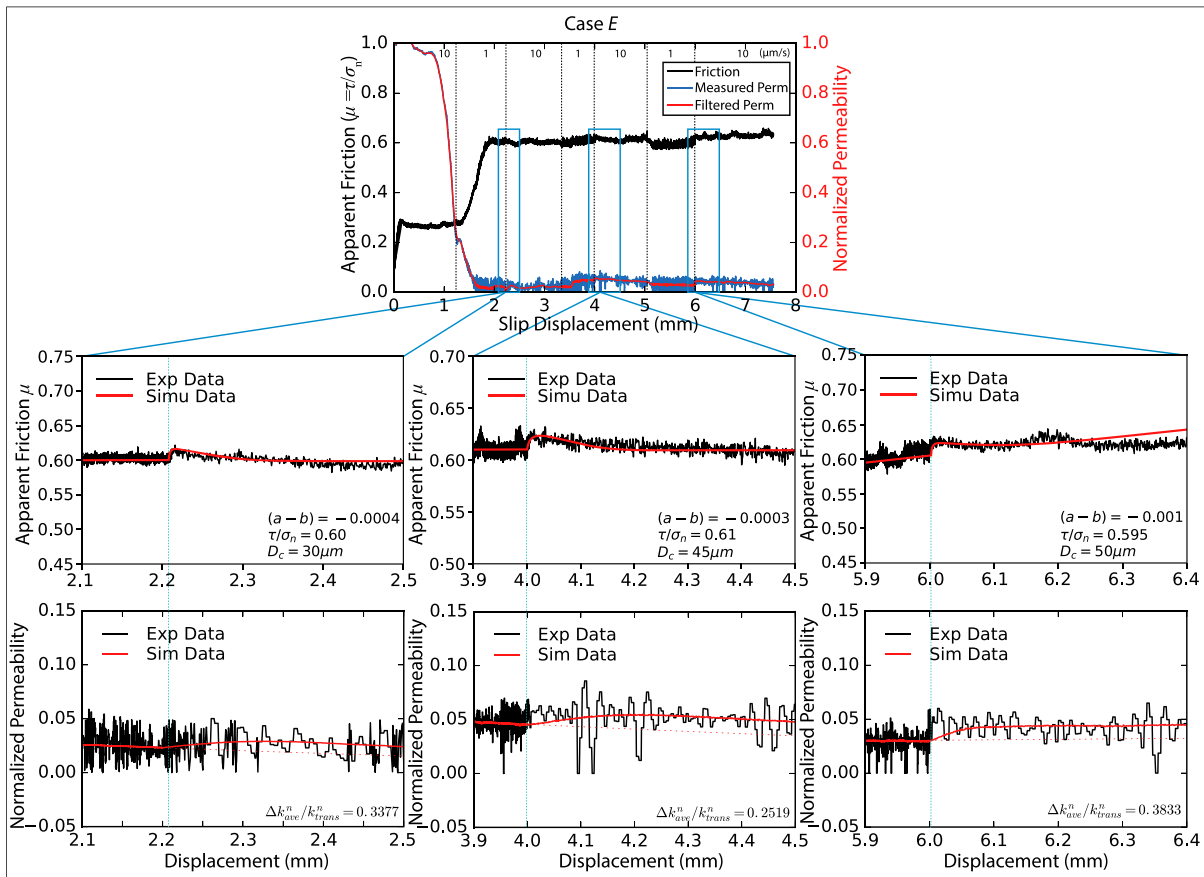
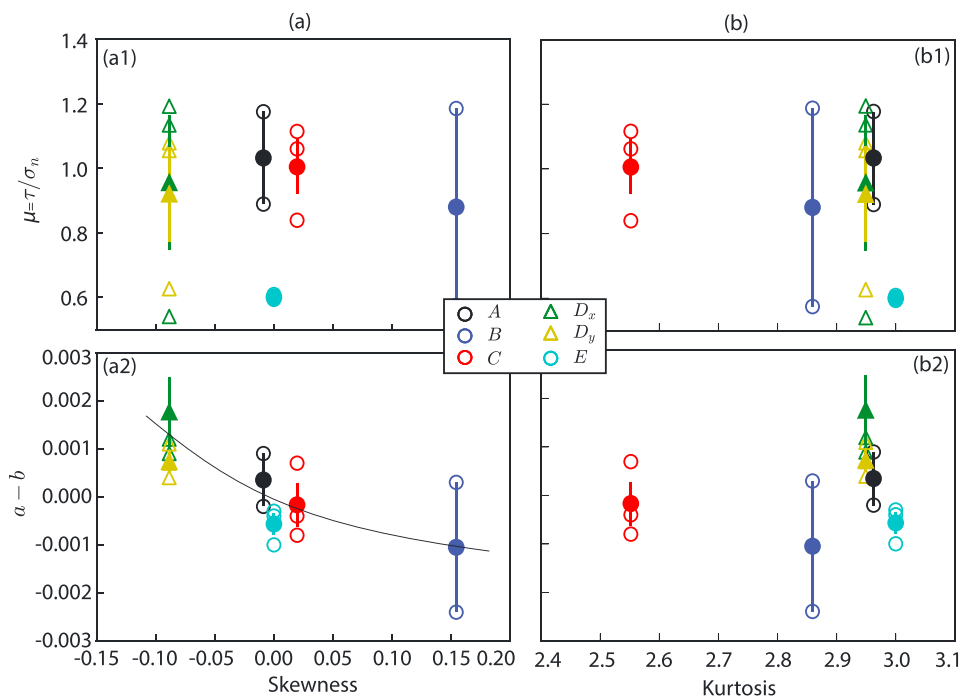


Figure A6. Friction-permeability data for fracture surface  $D_y$ . In each case data represent the friction response to an up-velocity step change in load point velocity.



**Figure A7.** Friction-permeability data for fracture surface *E*. In each case data represent the friction response to an up-velocity step change in load point velocity.



**Figure A8.** (a) Correlation of frictional parameters (i.e., apparent frictional strength and stability) and skewness; (b) correlation of frictional parameters and kurtosis.

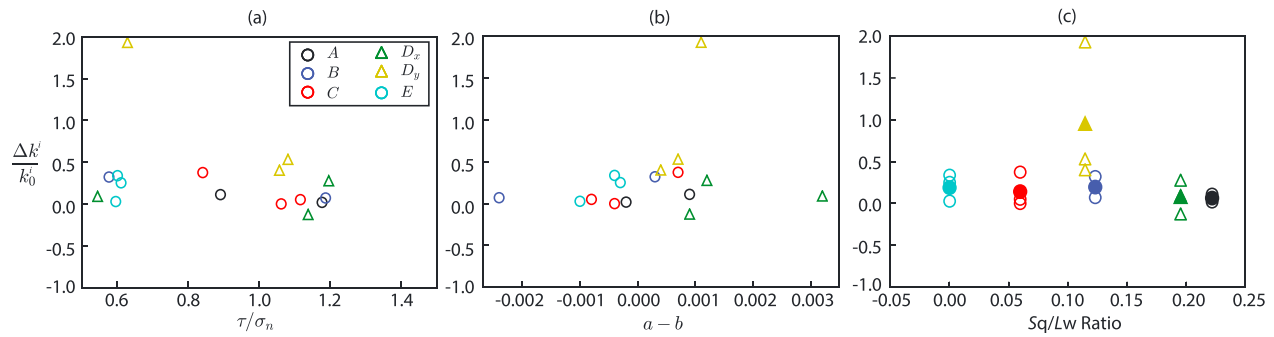


**Figure A9.** (a) Correlation of  $\Delta k^i/k_0^i$  and  $(\tau/\sigma_n)$  values; (b) correlation of  $\Delta k^i/k_0^i$  and  $(a-b)$  values. (c) Correlation of  $\Delta k^i/k_0^i$  and  $S_q/L_w$  ratio. The filled symbols refer to the average values of the unfilled symbols.

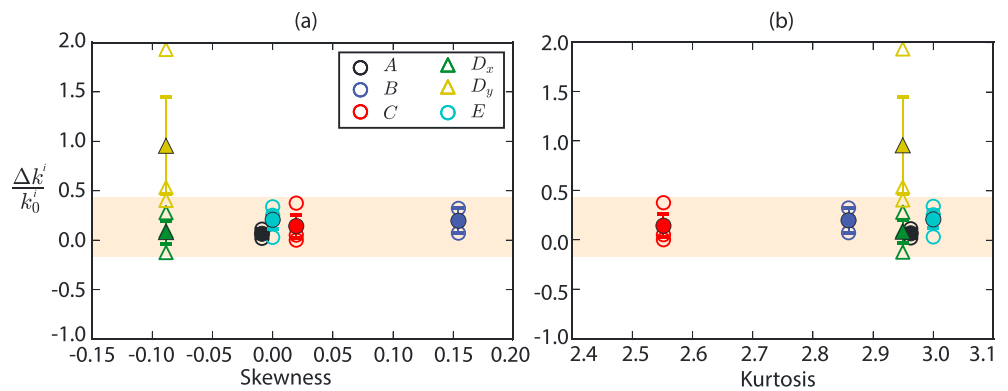


**Figure A10.** (a) Correlation of  $\Delta k^i/k_0^i$  and skewness values; (b) correlation of  $\Delta k^i/k_0^i$  and kurtosis values.

$$S_{sk} = \frac{1}{S_q^3 \cdot A} \iint_A z^3(x, y) dx dy \quad (A1)$$

The skewness measures the profile symmetry about the mean line. This dimensionless parameter can be positive (i.e., the bulk of asperities are below the mean line, suggesting a smoother surface) or negative (i.e., the bulk of asperities are above the mean line, suggesting a rougher surface). However, a rougher surface could also be zero when the Gaussian height distribution has a symmetrical topography. In such cases, it is necessary to examine kurtosis to confirm the roughness of a fracture with symmetrical topography.

The kurtosis is the ratio of the mean of the fourth power of the height values and the fourth power of  $S_q$  and provides a measure of the sharpness of the surface height distribution within the sampling area  $A$ ,

$$S_{ku} = \frac{1}{S_q^4 \cdot A} \iint_A z^4(x, y) dx dy \quad (A2)$$

Kurtosis is a positive and dimensionless value that measures the spread of the height distribution and determines whether the profile spikes are evenly distributed over the area. When a surface is featured as Gaussian height distribution, it has a kurtosis value of 3. If the kurtosis is smaller than 3, the surface is flat, while if the kurtosis is higher than 3, the surface has more peaks than valleys.

## References

- Akhavan, A., & Rajabipour, F. (2012). Quantifying the effects of crack width, tortuosity, and roughness on water permeability of cracked mortars. *Cement and Concrete Research*, 42(2), 313–320. <https://doi.org/10.1016/j.cemconres.2011.10.002>
- Asadi, M. S., Rasouli, V., & Barla, G. (2013). A laboratory shear cell used for simulation of shear strength and asperity degradation of rough rock fractures. *Rock Mechanics and Rock Engineering*, 46(4), 683–699. <https://doi.org/10.1007/s00603-012-0322-2>
- Barton, N. (1973). Review of a new shear-strength criterion for rock joints. *Engineering Geology*, 7(4), 287–332. [https://doi.org/10.1016/0013-7952\(73\)90013-6](https://doi.org/10.1016/0013-7952(73)90013-6)

## Acknowledgments

We thank the Editor Andre Revil and the Associate Editor Brandon Dugan for handling the manuscript and four anonymous reviewers whose careful reading and constructive comments helped improved the work. We thank Penn State Engineering Shop Services manager Ellis Dunklebarger for his help in 3-D printing. This work is the result of support provided by DOE Grant DE-FE0023354. This support is gratefully acknowledged. The data for this paper are listed in the table.

- Barton, N., Bandis, S., & Bakhtar, K. (1985). Strength, deformation and conductivity coupling of rock joints. *International Journal of Rock Mechanics and Mining Sciences*, 22(3), 121–140. [https://doi.org/10.1016/0148-9062\(85\)93227-9](https://doi.org/10.1016/0148-9062(85)93227-9)
- Barton, N., & Choubey, V. (1977). The shear strength of rock joints in theory and practice. *Rock Mechanics*, 10(1-2) 1–54. <https://doi.org/10.1007/BF01261801>
- Bear, J. (1988). *Dynamics of fluids in porous media*. New York: Dover Publications.
- Bletery, Q., Thomas, A. M., Rempel, A. W., Karlstrom, L., Sladen, A., & De Barros, L. (2016). Mega-earthquakes rupture flat megathrusts. *Science*, 354(6315), 1027–1031. <https://doi.org/10.1126/science.aag0482>
- Brodsky, E. E., Kirkpatrick, J. D., & Candela, T. (2016). Constraints from fault roughness on the scale-dependent strength of rocks. *Geology*, 44(1), 19–22. <https://doi.org/10.1130/G37206.1>
- Brown, S. R. (1995). Simple mathematical-model of a rough fracture. *Journal of Geophysical Research*, 100(B4), 5941–5952. <https://doi.org/10.1029/94JB03262>
- Cornet, F. H., Helm, J., Poitrenaud, H., & Etchecopar, a. (1997). Seismic and aseismic slips induced by large-scale fluid injections. *Pure and Applied Geophysics*, 150(3–4), 563–583. <https://doi.org/10.1007/s000240050093>
- Dieterich, J. H. (1978). Time-dependent friction and the mechanics of stick-slip. *Pure and Applied Geophysics PAGEOPH*, 116(4-5), 790–806. <https://doi.org/10.1007/BF00876539>
- Dieterich, J. H. (1979). Modeling of rock friction 1. Experimental results and constitutive equations. *Journal of Geophysical Research*, 84(B5), 2161–2168. <https://doi.org/10.1029/JB084iB05p02161>
- Ellsworth, W. L. (2013). Injection-induced earthquakes. *Science*, 341(6142), 142–149. <https://doi.org/10.1126/science.1225942>
- Elsworth, D., & Goodman, R. E. (1986). Characterization of rock fissure hydraulic conductivity using idealized wall roughness profiles. *International Journal of Rock Mechanics and Mining Science and Geomechanics Abstracts*, 23(3), 233–243. [https://doi.org/10.1016/0148-9062\(86\)90969-1](https://doi.org/10.1016/0148-9062(86)90969-1)
- Fang, Y., den Hartog, S. A. M., Elsworth, D., Marone, C., & Cladouhos, T. (2016). Anomalous distribution of microearthquakes in the Newberry Geothermal Reservoir: Mechanisms and implications. *Geothermics*, 63, 62–73. <https://doi.org/10.1016/j.geothermics.2015.04.005>
- Fang, Y., Elsworth, D., Wang, C., Ishibashi, T., & Fitts, J. P. (2017). Frictional stability-permeability relationships for fractures in shales. *Journal of Geophysical Research: Solid Earth*, 122, 1760–1776. <https://doi.org/10.1002/2016JB013435>
- Fang, Y., Elsworth, D., Wang, C., & Jia, Y. (2018). Mineralogical controls on frictional strength, stability, and shear permeability evolution of fractures. *Journal of Geophysical Research: Solid Earth*, 123, 3549–3563. <https://doi.org/10.1029/2017JB015338>
- Faoro, I., Niemeijer, A., Marone, C., & Elsworth, D. (2009). Influence of shear and deviatoric stress on the evolution of permeability in fractured rock. *Journal of Geophysical Research*, 114, B01201. <https://doi.org/10.1029/2007JB005372>
- Fung, A. K., Chen, K.-S., & Chen, K. S. (2010). Microwave scattering and emission models for users, Artech house.
- Gadelmawla, E. S., Koura, M. M., Maksoud, T. M. A., Elewa, I. M., & Soliman, H. H. (2002). Roughness parameters. *Journal of Materials Processing Technology*, 123(1), 133–145. [https://doi.org/10.1016/S0924-0136\(02\)00060-2](https://doi.org/10.1016/S0924-0136(02)00060-2)
- Guglielmi, Y., Cappa, F., Avouac, J.-P., Henry, P., & Elsworth, D. (2015). Seismicity triggered by fluid injection-induced aseismic slip. *Science*, 348(6240), 1224–1226. <https://doi.org/10.1126/science.aab0476>
- Harbord, C. W., Nielsen, S. B., De Paola, N., & Holdsworth, R. E. (2017). Earthquake nucleation on rough faults. *Geology*, 45(10), 931–934. <https://doi.org/10.1130/G39181.1>
- Huang, T. H., Chang, C. S., & Chao, C. Y. (2002). Experimental and mathematical modeling for fracture of rock joint with regular asperities. *Engineering Fracture Mechanics*, 69(17), 1977–1996. [https://doi.org/10.1016/S0013-7944\(02\)00072-3](https://doi.org/10.1016/S0013-7944(02)00072-3)
- Im, K., Elsworth, D., & Fang, Y. (2018). The influence of preslip sealing on the permeability evolution of fractures and faults. *Geophysical Research Letters*, 45, 166–175. <https://doi.org/10.1002/2017GL076216>
- Ishibashi, T., Watanabe, N., Asanuma, H., & Tsuchiya, N. (2016). Linking microearthquakes to fracture permeability change: The role of surface roughness. *Geophysical Research Letters*, 43, 7486–7493. <http://doi.org/10.1002/2016GL069478>
- Jaeger, J. C., Cook, N. G., & Zimmerman, R. W. (2007). *Fundamentals of Rock Mechanics* (4th ed.). Malden: Blackwell Publishing.
- Maini, Y. N. (1972). In situ hydraulic parameters in jointed rock: Their measurement and interpretation
- Majer, E. L., Baria, R., Stark, M., Oates, S., Bommer, J., Smith, B., & Asanuma, H. (2007). Induced seismicity associated with enhanced geothermal systems. *Geothermics*, 36(3), 185–222. <https://doi.org/10.1016/j.geothermics.2007.03.003>
- Marone, C., & Cox, S. J. D. (1994). Scaling of rock friction constitutive parameters: The effects of surface roughness and cumulative offset on friction of gabbro. *Pure and Applied Geophysics*, 143(1-3), 359–385. <https://doi.org/10.1007/BF00874335>
- Marsily, G. D. (1986). *Quantitative hydrogeology*, (1st ed.). San Diego: Academic Press.
- Moeck, I., Kwiatek, G., & Zimmermann, G. (2009). Slip tendency analysis, fault reactivation potential and induced seismicity in a deep geothermal reservoir. *Journal of Structural Geology*, 31(10), 1174–1182. <https://doi.org/10.1016/j.jsg.2009.06.012>
- Pereira, J. P., & De Freitas, M. H. (1993). Mechanisms of shear failure in artificial fractures of sandstone and their implication for models of hydromechanical coupling. *Rock Mechanics and Rock Engineering*, 26(3), 195–214. <https://doi.org/10.1007/BF01040115>
- Rice, J. R., & Ruina, A. L. (1983). Stability of steady frictional slipping. *Journal of Applied Mechanics*, 50(2), 343–349. <https://doi.org/10.1115/1.3167042>
- Ruina, A. (1983). Slip instability and state variable friction laws. *Journal of Geophysical Research*, 88(B12), 10,359–10,370. <https://doi.org/10.1029/JB088iB12p10359>
- Segall, P., & Fitzgerald, S. D. (1998). A note on induced stress changes in hydrocarbon and geothermal reservoirs. *Tectonophysics*, 289(1-3), 117–128. [https://doi.org/10.1016/S0040-1951\(97\)00311-9](https://doi.org/10.1016/S0040-1951(97)00311-9)
- Segall, P., & Rice, J. R. (1995). Dilatancy, compaction, and slip instability of a fluid-infiltrated fault. *Journal of Geophysical Research*, 100(B11), 22,155–22,171. <https://doi.org/10.1029/95jb02403>
- Talwani, P. (1997). On the nature of reservoir-induced seismicity. *Pure and Applied Geophysics*, 150(3–4), 473–492. <https://doi.org/10.1007/S000240050089>
- Tsang, Y. W. (1984). The effect of tortuosity on fluid flow through a single fracture. *Water Resources Research*, 20(9), 1209–1215. <https://doi.org/10.1029/WR020i09p01209>
- Walsh, F. R., & Zoback, M. D. (2015). Oklahoma's recent earthquakes and saltwater disposal. *Science Advances*, 1(5), e1500195. <https://doi.org/10.1126/sciadv.1500195>
- Wang, C., Elsworth, D., & Fang, Y. (2017). Influence of weakening minerals on ensemble strength and slip stability of faults. *Journal of Geophysical Research: Solid Earth*, 122, 7090–7110. <https://doi.org/10.1002/2016JB013687>
- Wang, K., & Bilek, S. L. (2014). Invited review paper: Fault creep caused by subduction of rough seafloor relief. *Tectonophysics*, 610, 1–24.
- Wu, W., Reece, J. S., Gensterblum, Y., & Zoback, M. D. (2017). Permeability evolution of slowly slipping faults in shale reservoirs. *Geophysical Research Letters*, 44, 11,368–11,375. <https://doi.org/10.1002/2017GL075506>

- Ye, Z., & Ghassemi, A. (2018). Injection-induced Shear Slip and Permeability Enhancement in Granite Fractures. *Journal of Geophysical Research: Solid Earth*, 123. <https://doi.org/10.1029/2018JB016045>
- Zoback, M. D., & Gorelick, S. M. (2012). Earthquake triggering and large-scale geologic storage of carbon dioxide. *Proceedings of the National Academy of Sciences of the United States of America*, 109(26), 10,164–10,168. <https://doi.org/10.1073/Pnas.1202473109>
- Zoback, M. D., Kohli, A., Das, I., & McClure, M. (2012). The importance of slow slip on faults during hydraulic fracturing stimulation of shale gas reservoirs, Spe 155476, (2011), SPE 155476. <https://doi.org/10.2118/155476-MS>